The Astrophysical Journal Letters, 993:L47 (9pp), 2025 November 10 https://doi.org/10.3847/2041-8213/ae160b

Mystery behind the Peeling of a Filament and the Associated Sudden Disappearance of a Sunspot Penumbra

Ju Jing[1,2], Mia Mancuso[1], Satoshi Inoue[1], Jeongwoo Lee[1], Qin Li[1], Wen He[1], Yan Xu[1,2], Wenda Cao[1,2], and Haimin Wang[1,2]

[1] Institute for Space Weather Sciences, New Jersey Institute of Technology, University Heights, Newark, NJ 07102-1982, USA; ju.jing@njit.edu
[2] Big Bear Solar Observatory, New Jersey Institute of Technology, 40386 North Shore Lane, Big Bear City, CA 92314-9672, USA

Received 2025 July 21; revised 2025 October 1; accepted 2025 October 17; published 2025 November 4

Abstract

On 2024 July 25, while observing the solar active region NOAA 13762 with the high-resolution 1.6 m Goode Solar Telescope at the Big Bear Solar Observatory, we witnessed two mysterious phenomena: the partial detachment of filament strands from its main body in the chromosphere and the sudden disappearance of a sunspot penumbra in the photosphere, the former accompanied by small flares. Our analysis reveals a spatiotemporal correlation between the filament peeling process and the penumbral disappearance. To understand the above observations physically, we performed a magnetohydrodynamic simulation that successfully replicated the disappearance of the penumbra as a consequence of weakened horizontal magnetic field. The simulations demonstrate that both the filament peeling and the penumbral decay are driven by the same underlying process: the upward expansion of the magnetic flux rope induced by null point magnetic reconnection. These results suggest a novel mechanism by which the Sun sheds magnetic flux to interplanetary space in the form of filament peeling and penumbral disappearance.

Unified Astronomy Thesaurus concepts: Sunspots (1653); Solar filament eruptions (1981); Solar magnetic reconnection (1504)

Materials only available in the online version of record: animations

1. Introduction

The Sun is our closest star and the only star whose surface features and diverse phenomena can be observed in detail—such as sunspots, filaments, and flares—spanning a broad spectrum of sizes, shapes, and evolutionary stages. Despite their apparent differences, all these features are fundamentally governed by the Sun's magnetic field. Consider sunspots, the focus of this study: these dark spots typically consist of a central dark umbra and a surrounding somewhat brighter filamentary penumbra, both of which are structured by magnetic fields: in the darkest umbra, the magnetic field is strongest and nearly vertical to the local solar surface, whereas in the surrounding lighter penumbra, the magnetic field is less intense, strongly inclined toward the surface so that it has a strong horizontal component of the magnetic field. Similarly, filaments—the elongated structures of the ionized plasma—are shaped and suspended by twisted magnetic flux ropes (MFRs). These features persist due to a delicate equilibrium of magnetic forces. However, when magnetic reconfiguration disrupts this balance, the filaments may undergo partial or full eruptions, often accompanied by solar flares.

Since the Sun's magnetic field governs both its surface features and dynamic activities of the Sun, and direct measurement of the Sun's three-dimensional (3D) magnetic field remains impossible, we rely on visible solar features and activities, combined with 3D magnetic field extrapolation techniques and magnetohydrodynamic (MHD) simulations, to understand the invisible solar magnetic field and its changes. The filamentary penumbra serves as an excellent example of this approach. Its structure implies a complex magnetic configuration often described as an "uncombed" (S. K. Solanki & C. A. P. Montavon 1993) or "interlocking comb" (J. H. Thomas & N. O. Weiss 2004) structure—the more horizontal magnetic components are interlaced with the more vertical magnetic components. Modern observations have confirmed the existence of varying inclinations in the penumbral magnetic field (e.g., H. Wang et al. 2012a), and recent radiative MHD simulations of sunspots have successfully reproduced not only the uncombed structure of the penumbral magnetic field but also flows and convective motions in the penumbra, which has significantly advanced our understanding of the physical processes occurring in the penumbra (e.g., M. Rempel 2011, 2015; A. L. Siu-Tapia et al. 2018).

Solar active regions typically evolve over timescales of days to months, with penumbral decay mirroring this time frame. Although the underlying mechanisms are not well understood, penumbra decay may be influenced by a variety of factors, such as magnetic cancellation, dispersion, and submergence, as well as interactions between the penumbra and moving magnetic features (V. Martínez Pillet 2002; M. Murabito et al. 2021; S. Idrees et al. 2024). However, active regions and sunspots are sometimes observed to undergo sudden and rapid changes within a timescale of a few minutes when a major flare occurs. Such sudden changes include (but are not limited to) the abrupt and sustained enhancement of the photospheric horizontal magnetic field near the central magnetic polarity inversion line (PIL; e.g., S. Wang et al. 2012b; H. Wang & C. Liu 2015; S. G. J. D. Petrie 2019; Toriumi & H. Wang 2019), the rapid enhancement of the central portion of the umbra, and the decay of the peripheral portion of the penumbra (e.g., H. Wang et al. 2004; N. Deng et al. 2005;

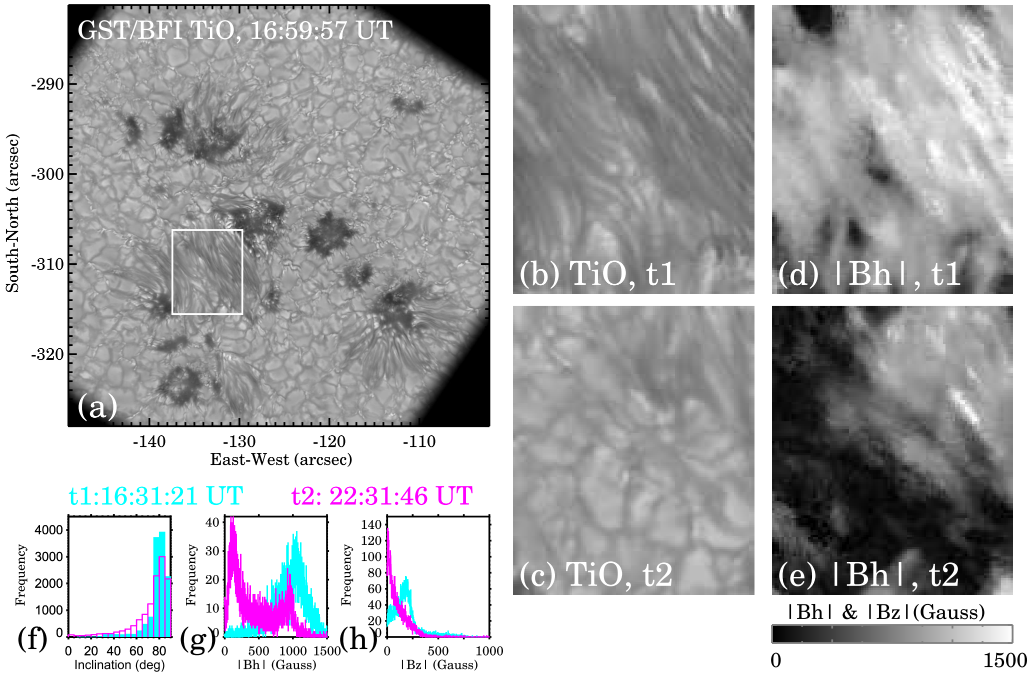

Figure 1. Disappearance of penumbra and changes in the penumbral magnetic field in the photosphere. (a) The GST TiO image taken at ∼17 UT, 2024 July 25. The box marks the FOV of the images shown in the panels (b)–(e). (b)–(c) The TiO images taken at the beginning and the end of the GST observation on that day, denoted by "t1" and "t2," respectively. The specific times for t1 and t2 are 16:31:21 UT and 22:31:47 UT, respectively. (d)–(e) GST/NIRIS horizontal magnetic field strength $|\boldsymbol{B}_h|$ at t1 and t2. (f)–(h) Histograms of magnetic inclination angle, $|\boldsymbol{B}_h|$, and $|\boldsymbol{B}_z|$ at t1 (cyan) and t2 (pink). The inclination angle is measured with respect to the local surface normal, i.e., 0° is vertical and 90° is horizontal. An animation of the TiO image sequence shows the evolution of the sunspot penumbra. The duration of the animation is 30 s.

(An animation of this figure is available in the online article.)

C. Liu et al. 2005; Y. Li et al. 2011; Z. Xu et al. 2016). These rapid penumbral changes are thought to represent a "back reaction" to solar eruptions (H. S. Hudson 2000; H. S. Hudson et al. 2008; G. H. Fisher et al. 2012) accompanied by an eruption-induced rearrangement of magnetic field lines. Specifically in the area where the peripheral penumbra suddenly weakens, the magnetic field may become more vertical following flare onset.

The advent of large-aperture solar telescopes in the recent decade enabled unprecedented high-resolution observations that reveal fine-scale structures and dynamic evolution of solar features. While these advancements provide invaluable insights into solar processes, they also present new challenges in deciphering the underlying magnetic drivers behind these complex phenomena. Recently, a high-resolution observation with the 1.6 m Goode Solar Telescope (GST; W. Cao et al. 2010; P. R. Goode & W. Cao 2012) at Big Bear Solar Observatory (BBSO) captured a previously unreported type of filament eruption: individual filament strands repeatedly peeling off from the main body of the filament, accompanied by flares (M. Mancuso et al. 2025). Due to the very fine scale of this peeling process—typically in the range of 100–300 km and only 1% of the total flux of the filament—it can only be seen at high resolutions. Physical causes for this phenomenon are under investigation, but it is probably related to magnetic reconnection between the filament strands.

Another recent high-resolution GST observation captured the peeling process of a filament, as well as the rapid disappearance of a sunspot penumbra. Whether or not the peeling of the filament and the disappearance of the penumbra are related to each other is of new interest. We therefore analyzed the observational data and performed appropriate MHD simulations to find an underlying driving mechanism for the two enigmatic phenomena.

2. Results

2.1. Observation

On 2024 July 25, the GST targeted the trailing part of the solar active region NOAA 13762, where a sunspot cluster was visible in the photosphere, and a filament meandering above the cluster was visible in the chromosphere. Two data sets, a photospheric TiO image sequence, and a chromospheric Hα image sequence, were successfully acquired, both spanning a time period of about 6 hr (16:31–22:31 UT).

Figure 1(a) shows a GST TiO image, where we can clearly see the filamentary penumbra between the sunspots. Of particular interest to us is the disappearance of the penumbra during the course of the observation. The region where the penumbra disappears is marked by the box in Figure 1(a). At the beginning of the observation, the penumbral structure covers almost the entire boxed region; over time, the penumbra fades away, revealing the photospheric granules underneath. Figures 1(b)–(g) show the TiO penumbra and the horizontal magnetic field strength $|\boldsymbol{B}_h|$ at the beginning (16:31 UT) and the end (22:31 UT) of the observation, respectively, in which $|\boldsymbol{B}_h|$ magnetograms were obtained from the Near-Infrared Imaging Spectropolarimeter (NIRIS; W. Cao et al. 2012) of GST. As mentioned earlier, a sunspot penumbra consists mainly of a horizontal magnetic field. A comparison between TiO and $|\boldsymbol{B}_h|$ images shows that the horizontal field is a good representation of the penumbra: it

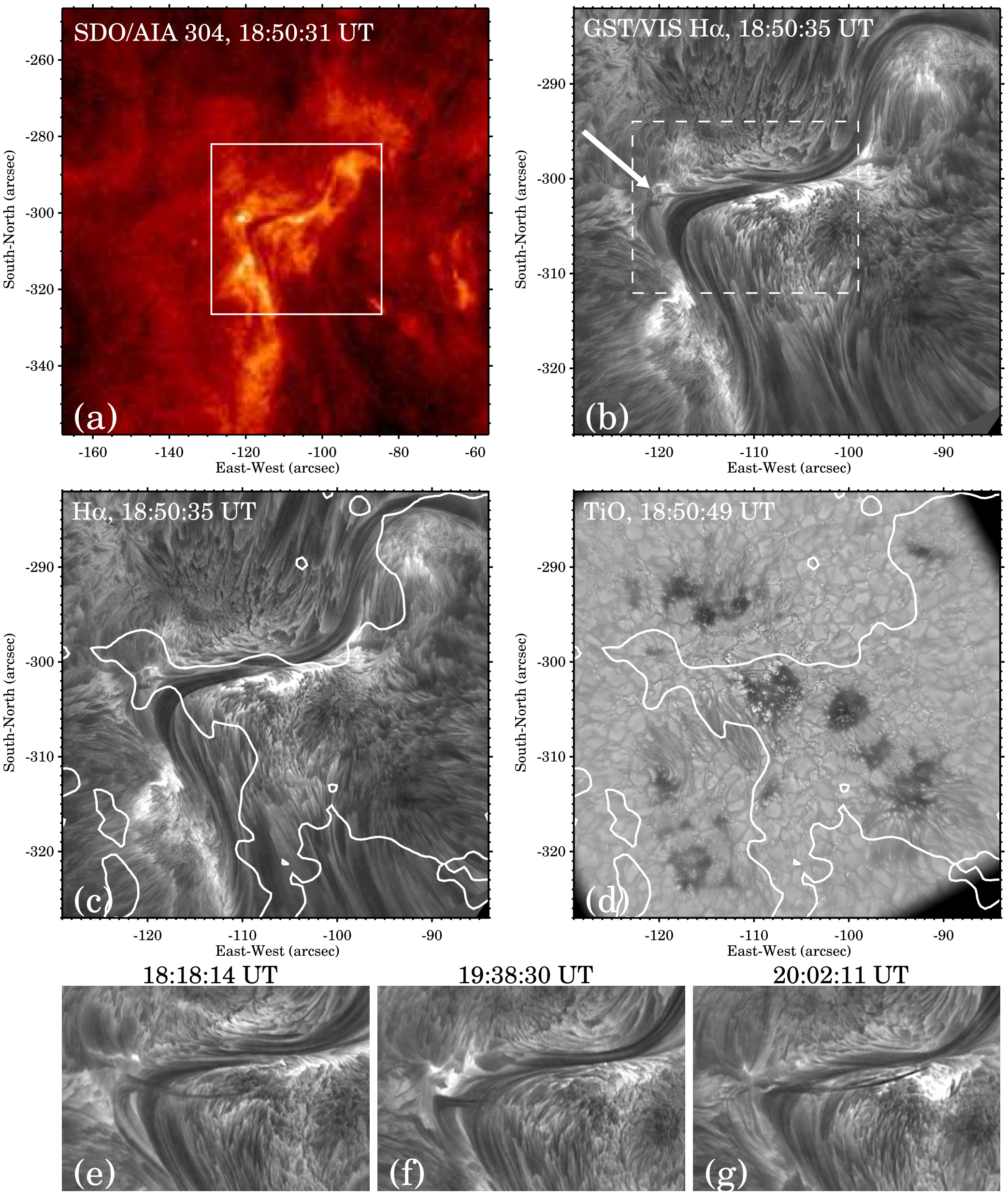

Figure 2. The filament and its peeling process in the chromosphere. (a) The SDO/AIA 304 Å image taken at ∼18:50 UT, where the box indicates the FOV of the GST Hα image shown in panel (b). (b) The GST chromospheric Hα image taken at ∼18:50 UT. The arrow points to a detached filament strand and the associated subflare. The dashed box indicates the FOV of the bottom panels (e)–(g). (c)–(d) The GST chromospheric Hα image and the photospheric TiO image, with the magnetic PILs superimposed on them. (e)–(f) Snapshots of the filament peeling at 18:18:14, 19:38:30, and 20:02:11 UT. An animation of the Hα image sequence shows the filament peeling process. The duration of the animation is 23 s.

(An animation of this figure is available in the online article.)

exhibits a filamentary structure similar to that of the penumbra, and, as the penumbra fades away, the horizontal magnetic field weakens significantly. The vertical field in the penumbra, on the other hand, is very weak relative to the horizontal magnetic field and is not shown here.

We then further quantitatively compare the histograms of the penumbral magnetic field at these two moments. Figures 1(f)–(h) show the magnetic inclination angle histograms, $|\boldsymbol{B}_h|$ histograms, and $|\boldsymbol{B}_z|$ histograms at these two times, respectively. From 16:31 to 22:31 UT, there is a decrease in the number of highly inclined magnetic fields in the penumbra, suggesting that the penumbral field becomes more vertical. It is also clear that the overall distributions of both $|\boldsymbol{B}_h|$ and $|\boldsymbol{B}_z|$ are shifted toward weaker field strengths with time, indicating that both horizontal and vertical magnetic fields in the penumbra are weakening with time. If the disappearance of the penumbra is simply due to a change in the magnetic field from more horizontal to more vertical, then we should see that $|\boldsymbol{B}_h|$ weakens over time while $|\boldsymbol{B}_z|$ strengthens. Though the horizontal magnetic field is compatible with this expectation, the change in the vertical magnetic field is not. It thus seems that the disappearance of the penumbra cannot be explained simply by a change in the magnetic field inclination; other mechanisms should be involved. We will return to this issue in the simulation section (Section 2.2).

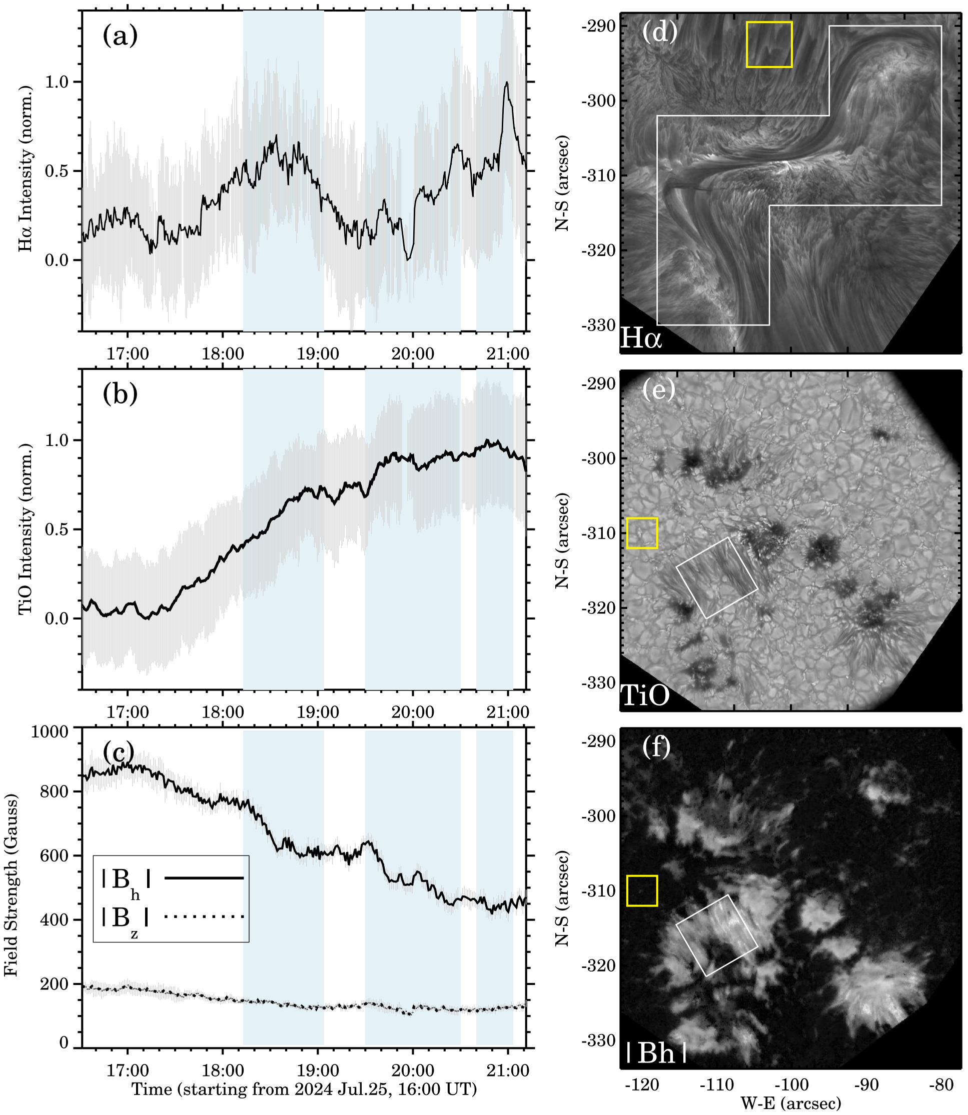

Figure 3. The temporal correlation between the penumbra disappearance and the filament peeling. (a) Time evolution of the normalized Hα intensity (averaged over the white polygon region in (d)). (b) Time evolution of the normalized TiO intensity (averaged over the white boxed region in (e)). (c) Time evolutions of $|\boldsymbol{B}_h|$ and $|\boldsymbol{B}_z|$ (both averaged over the white boxed region in (f)). Gray error bars represent the standard deviation calculated from a quiescent region shown as the yellow boxed region in the corresponding image. The shaded regions in (a)–(c) indicate the periods in which filament peeling occurs intensively. (d)–(f) The images of GST Hα, TiO, and horizontal magnetic field strength taken at about 18:21 UT, with the white and yellow boxes defining the regions where the Hα intensity, TiO intensity, and magnetic field strength and their uncertainties are computed, respectively. An animation of the evolution of photospheric magnetic field is available. The animation lasts 16 s, with the left and right panels showing vertical and horizontal photospheric magnetograms, respectively.

(An animation of this figure is available in the online article.)

Changes occur not only in the photosphere but also in the chromosphere. Figure 2(a) shows a larger field-of-view (FOV) chromospheric image taken by the Atmospheric Image Assembly (AIA; J. R. Lemen et al. 2012) on board the Solar Dynamic Observatory (SDO) at He II 304 Å. We can vaguely see a filament with some brightenings around it. We call these brightenings "subflares" because they are not strong enough to be classified as official flare events, but they are, like official flares, a manifestation of the sudden release of energy stored in the magnetic field. Figure 2(b) shows a high-resolution GST chromospheric Hα image, which clearly reveals the fine structure of the filament and the surrounding subflares. This filament, roughly V shaped, appears to be composed of many fine strands, tracing the MFR that holds the dense plasma together. The middle panels (c) and (d) place the chromospheric Hα and photospheric TiO images side by side with the magnetic PIL superimposed on them, which helps us to relate the positions of the sunspots and the filament overlying the sunspots. From the animation of the Hα image sequence, we can see that individual strands have peeled off from the main body of the filament several times during the observation, until a relatively larger eruption occurred at ~20:45 UT. One such peeling is captured in Figure 2(b)—just at the turning point of the V-shaped filament, a strand is detaching from the filament, accompanied by a very small subflare (indicated by the arrow) as well as other subflares around the filament. Based on observations, this turning point of the V shape seems to be the main location for the filament peeling, as evidenced by its examples at other moments; see Figures 2(e)–(g).

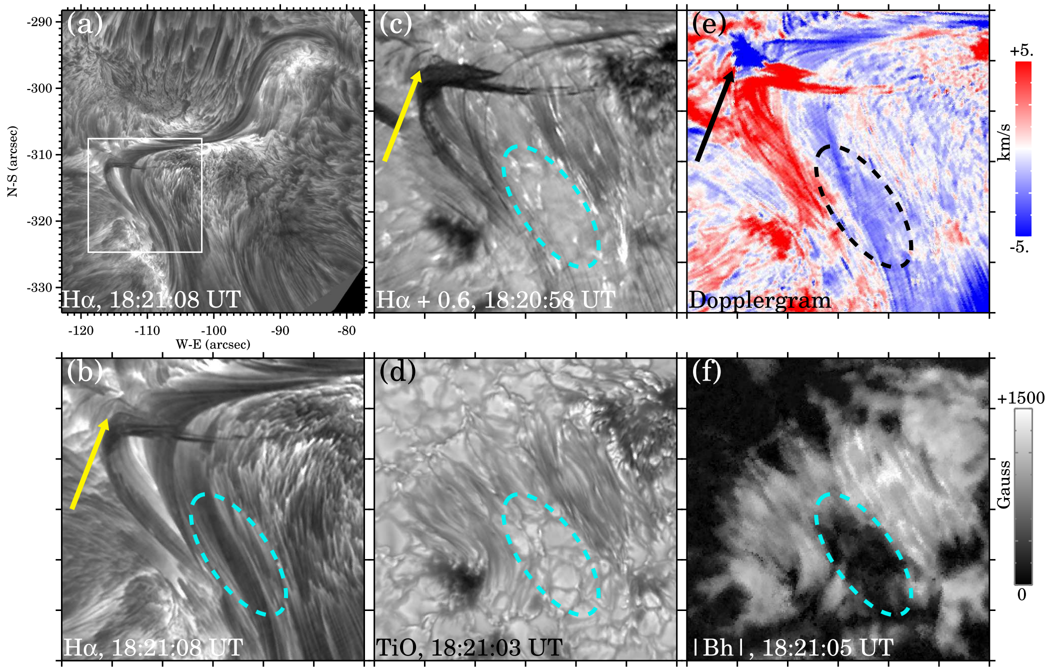

Figure 4. The spatial correlation between the penumbra disappearance and the filament peeling. (a) GST Hα image taken at 18:21 UT. The box marks a region of interest for the close-up views shown in panels (b)–(f). (b)–(f) The GST images of the Hα center line, Hα+0.6 Å, TiO, Dopplergram, and horizontal field strength $|\boldsymbol{B}_h|$, all obtained approximately at 18:21 UT. The arrows in these panels point to a strand peeling off from the main body of the filament, and the ovals highlight the area where the penumbra disappears significantly.

To better relate the disappearing penumbra in the photosphere to the filament peeling in the chromosphere, we investigated their temporal and spatial correlations, which are shown in Figures 3 and 4, respectively. Specifically, the following time profiles are shown in Figure 3: (a) Hα intensity around the filament; (b) TiO intensity in the penumbra; and (c) $|\boldsymbol{B}_h|$ and $|\boldsymbol{B}_z|$ in the penumbra. The shaded areas in Figures 3(a)–(c) indicate the periods in which the filament peeling occurs continuously or intensively. The peaks in (a) indicate subflares of varying magnitude, with two relatively strong subflares occurring roughly around 18:30 and 21:00 UT, both associated with the filament peeling process; the increase in TiO intensity in (b) indicates that more and more penumbral regions are taken over by brighter granular regions (i.e., disappearance of the penumbra); and the decrease of the curves in (c) indicates the weakening of the magnetic field with time, with the horizontal magnetic field dominating. The disappearance of the penumbra and the weakening of the magnetic field began at about 17:10 UT, an hour before the earliest recognizable filament peeling, but the most significant weakening of the magnetic field occurs during the periods of filament peeling, especially the first period. The weakening trend of the penumbral horizontal field is much more pronounced than that of the vertical field.

Figure 4 shows a set of images obtained at approximately 18:21 UT, during the first filament peeling period. These images include Hα line center, Hα off band (+0.6 Å), TiO, Dopplergram, and horizontal field strength $|\boldsymbol{B}_h|$, in which the Hα off-band image displays features of both chromospheric filaments and photospheric sunspots, and the Dopplergram shows the Doppler velocity of plasma motions toward or away from the observer (i.e., upward or downward motion). As can be seen in Figure 4, the peeling of the filament occurs at the turning point of the V-shaped filament, and one edge of the V overlaps with the region where the penumbra disappears. In the region where the penumbra disappears, the Dopplergram shows an absolute dominance of blueshift, indicating an upward motion. The detached filament strands, on the other hand, are both blueshifted and redshifted: a strong blueshift (upward motion) is evident at the turning point (the tip) of the V-shaped detached strand, while the rest of the detached strand is redshifted (downward motion). The redshift outside the tip of the peeled strand may be due to the "mass-draining" effect in the early stage of the eruption, whereby material is drained downward along the rising field lines by the downward magnetic and gravitational forces, further increasing the height of the rising field lines to reach a new equilibrium, or leading to a successful eruption (J. M. Jenkins et al. 2019).

2.2. Simulation

Since the disappearance of the penumbra and the filament peeling process are related in both time and space, the question arises: By what physical process are they linked?

In order to answer this question, we performed an MHD simulation using the nonlinear force-free field (NLFFF) extrapolated from the photospheric magnetic field (at 17 UT) as the initial condition. Since the NLFFF model and subsequent simulations require a large FOV, we used the photospheric magnetograms obtained by the Heliospheric and Magnetic Imager (HMI; J. Schou et al. 2012) of SDO, instead of the smaller FOV NIRIS magnetograms, as boundary conditions. Figure 5 shows the presence of a V-shaped MFR in the NLFFF model, whose overall shape and location are nearly identical to that of the Hα filament. When passing through the penumbral region, this MFR is very low-lying and almost tangent to the surface. Note that, at the turning point of the V-shaped MFR where the filament peeling is observed, there is a magnetic null point (NP), which is often regarded as the primary site for magnetic reconnection.

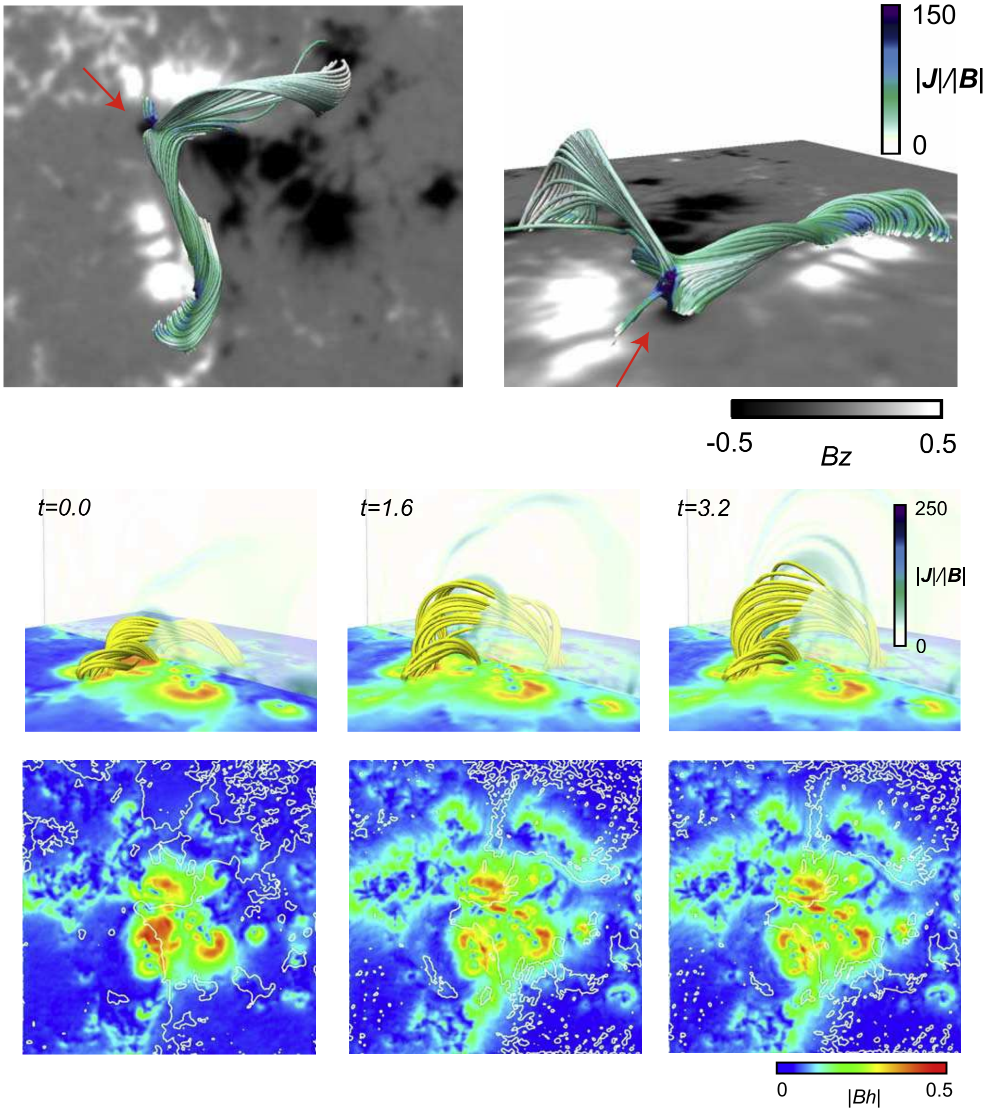

Figure 5. The MFR in the NLFFF model and the MHD simulation of magnetic field evolution. Top two panels: top and side views of the MFR, superimposed on the HMI photospheric $\boldsymbol{B}_z$ map taken at 17 UT. The red arrow indicates the location of the magnetic NP. Middle panels: simulated 3D magnetic field lines (with vertical cross sections of $|\boldsymbol{J}|/|\boldsymbol{B}|$) at Alfvén time $t = 0.0$, 1.6, and 3.2. Bottom panels: the top views of simulated horizontal magnetic field strengths in the photospheric layer (at an altitude of ∼400 km) at $t = 0.0$, 1.6, and 3.2. The color bar values for $\boldsymbol{B}_z$ and $|\boldsymbol{B}_h|$ represent percentages relative to their maximum values.

The MHD simulation was performed under the zero-beta approximation (see, for details, Appendix A.2.2), which introduces several important limitations. First, omission of gravity prevents the simulation from capturing dynamics such as plasma draining or sedimentation. Second, the absence of the pressure gradient term in the momentum equation negates the effects of possible enhancements of density or temperature within filaments. Furthermore, the thermal energy from magnetic reconnection is dissipated directly rather than being fed back into the plasma. These limitations should be considered when interpreting the simulation results.

The simulation shows that magnetic reconnection between the MFR field lines does occur at the NP, forming longer field lines and disrupting the force balance that maintains MFR stability. This destabilization triggers an upward expansion of the MFR, which lifts portions of the previously low-lying penumbral magnetic field from the photosphere. Consequently, both the horizontal and vertical magnetic field components show localized weakening in the photosphere. The middle and bottom panels of Figure 5 illustrate this process, showing the expansion of the simulated field line and its photospheric impact. The simulated time profiles of the penumbral fields in Figure 6 show field strength reductions of 34% in $|\boldsymbol{B}_h|$ and 9% in $|\boldsymbol{B}_z|$. These values are qualitatively matching observed trends though with weaker magnitude than the 50% $|\boldsymbol{B}_h|$ and 28% $|\boldsymbol{B}_z|$ decreases measured by the high-resolution NIRIS magnetograms.

These simulation results directly address the question posed in Section 2.1 about alternative mechanisms for penumbral disappearance. The model demonstrates that the vanishing penumbral signature arises not merely from changes in magnetic field inclination but from the upward expansion of the penumbral magnetic field and plasma, which renders the penumbra invisible at the photospheric level. The upward expansion of the MFR is also supported by Dopplergram measurements (Figure 4(e)) in the region of penumbral decay. This simulation cannot fully reproduce the filament peeling process, as it requires both higher-resolution magnetograms and a more refined modeling of filaments involving low-density plasma beyond the model capability. However, the

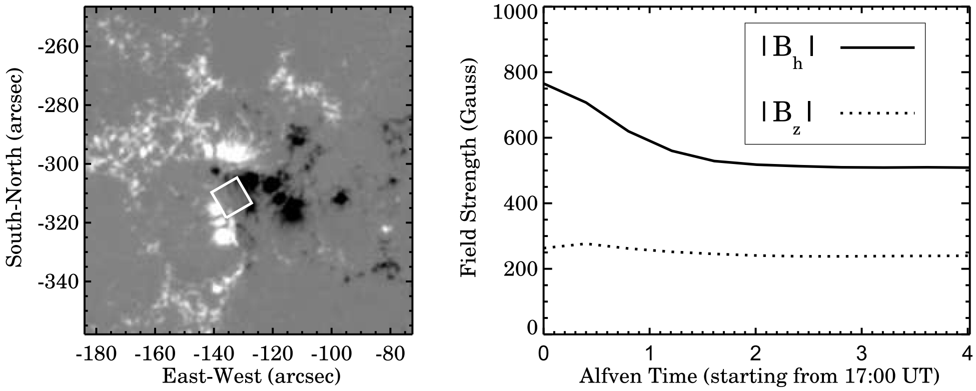

Figure 6. The evolution of penumbral horizontal and vertical field strength in the simulation. Left: HMI B_z map at 17:00 UT, showing the FOV of the bottom boundary of the NLFFF model and the simulation. The box indicates the region of penumbra disappearance, which is the same as the region shown by the box in Figure 3(f). Right: time profiles of $|\boldsymbol{B}_h|$ (solid) and $|\boldsymbol{B}_z|$ (dotted), averaged over the boxed region shown in the left panel. The simulation time "0" corresponds to 17:00 UT.

current model result confirms the existence of magnetic reconnection within the MFR, which may trigger the filament peeling.

3. Conclusion

On 2024 July 25, high-resolution solar observations with GST captured two remarkable phenomena: the peeling of the filament in the chromosphere and the disappearance of the penumbra in the photosphere. As a newly discovered form of filament activity, reported only once to date (M. Mancuso et al. 2025), the triggering mechanism for the filament peeling, its occurrence rate, and space weather implications are entirely unknown. M. Mancuso et al. (2025) proposed that internal magnetic reconnection between filament threads could be a trigger, but this remained a speculative hypothesis. Our simulation supports this mechanism in that internal reconnection of the MFR's field lines is likely to prompt the peeling process. A further insight is that filament peeling and penumbral disappearance, observed concurrently in our event, likely share a common physical driver: the upward expansion of an MFR initiated by magnetic reconnection.

Although penumbral disappearance has been frequently associated with flares, the event presented here is distinct from previous reports and points to a novel process by which the Sun sheds magnetic flux into interplanetary space. In the previous cases (e.g., N. Deng et al. 2005; C. Liu et al. 2005; Z. Xu et al. 2016), the rapid disappearance of the penumbra occurs predominantly in the outer penumbra, well separated from the magnetic PIL, and is linked to the local field lines becoming more vertical, as a consequence of the back reaction of the eruption impacting the photosphere. In contrast, this sudden disappearance of the penumbra occurs around the main magnetic PIL, and there are no major eruptions throughout. The phenomenon cannot be attributed to the photospheric back reaction of a coronal mass eruption. Instead, our observations and simulations indicate that localized magnetic reconnection drives the upward expansion of the MFR, which in turn causes the penumbral decay through field line restructuring. Slow penumbral disappearance is also found in the remnant of a decaying penumbra through spectropolarimetric measurements and attributed to the buoyancy-induced rise of the penumbral field (L. R. Bellot Rubio et al. 2008). The slow penumbral decay (occurring over ∼3 days) and the rapid disappearance (within hours) studied here share similar photospheric signatures—both involve the rising and vanishing of penumbral structures. However, their distinct timescales point to fundamentally different driving mechanisms: gradual buoyancy forces dominate the slow decay, while impulsive magnetic reconnection drives the rapid event. These observations demonstrate an important diversity in penumbral disappearance phenomena, revealing how different physical processes can produce morphologically similar but kinematically distinct evolutions.

Acknowledgments

We thank the referee for the critical and helpful comments to improve this Letter. We gratefully acknowledge the use of data from the Goode Solar Telescope (GST) of the Big Bear Solar Observatory (BBSO). BBSO operation is supported by US NSF AGS-2309939 and New Jersey Institute of Technology. GST operation is partly supported by the Korea Astronomy and Space Science Institute and Seoul National University. We thank the NASA SDO team for HMI and AIA data. HMI and AIA are instruments on board SDO, a mission for NASA's Living with a Star program. This study is supported by NASA grants 80NSSC23K0406, 80NSSC24K0258, 80NSSC21K1671, 80NSSC21K0003, 80NSSC24K1914, and 80NSSC24M0174 and NSF grants AST-2108235, AGS-2114201, 2145253, 2149748, 2206424, 2300341, 2309939, 2401229 and 2408174.

Appendix
Methods

A.1. Data

The GST is a ground-based 1.6 m aperture off-axis solar telescope at the BBSO. Equipped with a high-order adaptive optics system and with the aid of the post facto speckle image reconstruction technique, GST is able to achieve diffraction-limited imaging of the Sun. Photospheric TiO (7057 Å) and chromospheric Hα (6563 Å and its off-band) images, obtained by GST's Broadband Filter Imager and GST's Visible Imaging Spectrometer (VIS), respectively, are used in this Letter to study the evolution of the sunspot penumbra in the photosphere and the filament in the chromosphere, respectively. Specifically for this observation, VIS scanned the target area at 11 wavelengths (±1.0, ±0.8, ±0.6, ±0.4, ±0.2, and 0.0 Å from the Hα line center). At each wavelength step, 60 frames were taken in rapid succession, and the 25 frames with the best contrast were saved. The TiO and Hα images have a spatial sampling of $\sim 0\rlap{.}''03$ per pixel, and both span a time period of about 6 hr (16:30–22:30 UT) at a cadence of 34–38 s. The time series of the images were aligned with the optical flow method and the scale-invariant feature transform (D. D. Lowe 2004) method, which were implemented by a Python language package developed specifically for GST imaging data (X. Yang et al. 2022).

To obtain the Dopplergram, images in each Hα wavelength were normalized by the exposure time and calibrated to match its average intensity to the standard solar Hα profiles from https://bass2000.obspm.fr. At every point in the images, a set of 11 wavelength intensities was used to calculate the so-called center-of-gravity wavelength defined as the centroid of the residual intensities of the continuum intensity as the reference profile (H. Uitenbroek 2003), and its difference from the line center wavelength gives the local Doppler velocity. The Dopplergram shown in Figure 4(e) was obtained using the 11 wavelength point images taken at ∼18:21 UT.

To study the evolution of the photospheric magnetic field, we used the spectropolarimetric data at the 1.56 μm Fe I line obtained with GST's NIRIS. The spectropolarimetric data were processed with the NIRIS data processing pipeline (K. Ahn et al. 2016), including dark and flat field correction, calibration of instrumental crosstalk, and Milne–Eddington Stokes inversion. For this data set, we employed a new method of spectropolarimetric inversions based on physics-informed neural networks to infer the photospheric vector magnetic field under the Milne–Eddington approximation (R. Jarolim et al. 2025). The NIRIS vector magnetograms have a spatial sampling of $0\rlap{.}''08$ per pixel and a temporal cadence of ∼62 s for this observation. Since the sunspot penumbra is close to the center of the solar disk, we approximate the line-of-sight and transverse magnetic fields observed in the image plane as the vertical and horizontal magnetic fields in the heliographic plane.

In addition, we also used SDO/HMI photospheric vector magnetograms, with a spatial sampling of $0\rlap{.}''5$, as boundary conditions to extrapolate the NLFFF model and perform the MHD simulation. The reason why we used HMI magnetograms instead of high-resolution NIRIS magnetograms as boundary conditions is that NIRIS magnetograms have a smaller FOV and are therefore not suitable for studying the evolution of the MFR. The HMI data centered on the region of interest were transformed to a local Cartesian coordinate system using the same cylindrical equal area (CEA) projection that is used to produce the standard HMI Space-weather HMI Active Region Patches CEA data series.

A.2. *NLFFF Extrapolation and MHD Simulation*

A.2.1. *NLFFF Extrapolation*

We employ the following equations to carry out an NLFFF extrapolation (S. Inoue 2016):

$$\rho = |\boldsymbol{B}|, \tag{A1}$$

$$\frac{\partial \boldsymbol{v}}{\partial t} = \frac{1}{\rho}\boldsymbol{J} \times \boldsymbol{B} - \nu_f \boldsymbol{v}, \tag{A2}$$

$$\frac{\partial \boldsymbol{B}}{\partial t} = \boldsymbol{\nabla} \times (\boldsymbol{v} \times \boldsymbol{B}) + \eta \boldsymbol{\nabla}^2 \boldsymbol{B} - \boldsymbol{\nabla}\phi, \tag{A3}$$

$$\boldsymbol{J} = \boldsymbol{\nabla} \times \boldsymbol{B}, \tag{A4}$$

$$\frac{\partial \phi}{\partial t} + c_h^2 \boldsymbol{\nabla} \cdot \boldsymbol{B} = -\frac{c_h^2}{c_p^2}\phi, \tag{A5}$$

where $\boldsymbol{B}$ is the magnetic flux density, $\boldsymbol{v}$ is the velocity, $\boldsymbol{J}$ is the electric current density, ρ is the plasma density, and ϕ is a convenient scalar potential for reducing the errors in $\boldsymbol{\nabla} \cdot \boldsymbol{B}$ (A. Dedner et al. 2002). The length, magnetic field, density, velocity, and time are normalized by $L^* = 82(Mm)$, $B^* = 0.20(T)$, and $\rho^*(\text{kg m}^3)$, which is the density at the bottom surface, $V_\text{A}^* \equiv B^*/(\mu_0 \rho^*)^{1/2}$, where μ_0 is the magnetic permeability in free space, and $\tau_\text{A}^* \equiv L^*/V_\text{A}^*$. The space derivative is approximated by the second-order central differential method, and the Runge–Kutta–Gill method is applied to time integration. The coefficients c_h^2 and c_p^2 in Equation (A5) are set with values 0.04 and 0.1, respectively. The coefficients ν_f and η correspond to a friction coefficient and an electrical resistivity. The friction coefficient sets $\nu_f = 1.0$ and the resistivity sets $\eta = 5.0 \times 10^{-5} + 1.0 \times 10^{-2} |\boldsymbol{J} \times \boldsymbol{B}||\boldsymbol{v}|^2/|\boldsymbol{B}|^{\boldsymbol{2}}$ are given to converge to the NLFFF quickly in weak magnetic field regions.

The potential field, derived from the normal component of the boundary (T. Sakurai 1982), was used as the initial condition. We then iterated the above equations until the magnetic field reached a near-equilibrium state, namely the NLFFF (S. Inoue 2016). During the iteration, the normal component at the bottom surface was fixed over time, while the tangential components followed the equation, $\boldsymbol{B}_t = \gamma \boldsymbol{B}_\text{obs} + (\gamma - 1)\boldsymbol{B}_\text{pot}$, where the $\boldsymbol{B}_t$, $\boldsymbol{B}_\text{obs}$, and $\boldsymbol{B}_\text{pot}$ represent the tangential components of the magnetic field, the observed magnetic field, and the potential field, respectively. γ ranges from 0 to 1, and when $\gamma = 1$, $\boldsymbol{B}_t$ exactly matches $\boldsymbol{B}_\text{obs}$. During the iteration, if $R = \int |\boldsymbol{J} \times \boldsymbol{B}|^2 dV$, calculated over the interior of the computational domain, falls below a critical value denoted by R_min, the parameter γ is increased by $d\gamma$, i.e., $\gamma = \gamma + \text{d}\gamma$. In this paper, R_min and $d\gamma$ had the values 1.0×10^{-2} and 2.0×10^{-2}, respectively. At the other boundaries, each normal magnetic field component was fixed over time, while each horizontal component evolved in the induction equation. The velocity was set to zero, and $\partial\phi/\partial t = 0$ was imposed at all boundaries.

In this calculation, we assume the normalized density as $\rho(\boldsymbol{r}, t) = |\boldsymbol{B}(\boldsymbol{r}, t)|$ to ease the relaxation of the simulation by equalizing the Alfvén speed in space. In order to avoid undesired sudden jumps near the boundary during the iterations, the velocity is adjusted as follows, $\boldsymbol{v} \Leftarrow \min(1, 0.04/M_\text{A})\boldsymbol{v}$, where $M_\text{A} \equiv |\boldsymbol{v}|/|\boldsymbol{v}_\text{A}|$ is the Alfvén Mach number. The velocity is limited $0.04 M_\text{A}$ or less. The NLFFF extrapolation is applied to the photospheric magnetic field observed at 17:00 UT, before the disappearance of penumbra and the onset of filament peeling.

A.2.2. *MHD Simulation*

We performed MHD simulations using the above NLFFFs as the initial condition employing the zero-beta approximation implemented by S. Inoue et al. (2014) and S. Inoue (2016). Although our computational domain encompasses both chromospheric and coronal regions and this approximation neglects plasma pressure effects, we emphasize that the primary phenomena under investigation—penumbral decay and magnetic reconnection within the filament—are magnetically driven in the low-beta corona. Therefore, we anticipate that the essential dynamics remain largely unaffected by this simplification.

The equations of motion are similar to those used in the NLFFF extrapolation. However, the momentum Equation (A2) is replaced by

$$\frac{\partial \boldsymbol{v}}{\partial t} = -\boldsymbol{v} \cdot \nabla \boldsymbol{v} + \frac{1}{\rho}\boldsymbol{J} \times \boldsymbol{B} - \nu \nabla^2 \boldsymbol{v}, \tag{A6}$$

where the viscosity ν is set to 2.5×10^{-4}. Here the inertial term is added, which is unimportant in getting the static solution, but becomes important in MHD simulation, especially when the velocity rapidly increases under MHD instabilities. It is ideal to add the pressure gradient term here. However, incorporating the gas pressure is technically challenging because the pressure distribution is not directly constrained by observations. As a result, one must assume the initial and boundary conditions for the pressure term in an arbitrary manner, which may lead to nonphysical results.

The Equation (A3) remains the same except that we use an anomalous electrical resistivity in the following form:

$$\eta = \begin{cases} \eta_0 & J < j_c, \\ \eta_0 + \eta_1 \left(\frac{J - j_c}{j_c}\right)^2 & J > j_c, \end{cases} \tag{A7}$$

where dimensionless background resistivities η_0 and η_1 are set to 1.0×10^{-5} and 1.0×10^{-3}, respectively. The dimensionless resistivity used in this simulation is defined as $\eta/(L_0 V_A)$, with $L_0 = 1.0 \times 10^8$ m and $V_A = 1.0 \times 10^6\ \mathrm{m\ s^{-1}}$, representing dimension and Alfvénic speed in the corona. Accordingly, the dimensional values of η_0 and η_1 can be recovered by multiplying by $10^{14}\ \mathrm{m^2\ s^{-1}}$ and then multiplying by their respective dimensionless values. J is the magnitude of the electric current density, and j_c is the threshold current, which was set to 60 in this study. This form of anomalous electrical resistivity is introduced to reflect magnetic reconnection enhanced in strong current density. The boundary condition was the same as the NLFFF, except that all three components of the magnetic field are fixed from the beginning of the calculation. This was done to investigate the variation of the tangential components in the lower corona without altering the bottom condition.

Both the NLFFF and MHD simulations were performed in the volume of $\sim 82 \times 82 \times 82\ \mathrm{Mm}^3$, which was divided into $224 \times 224 \times 224$ grids.

ORCID iDs

Ju Jing https://orcid.org/0000-0002-8179-3625
Mia Mancuso https://orcid.org/0009-0004-9313-6173
Satoshi Inoue https://orcid.org/0000-0001-5121-5122
Jeongwoo Lee https://orcid.org/0000-0002-5865-7924
Wenda Cao https://orcid.org/0000-0003-2427-6047
Haimin Wang https://orcid.org/0000-0002-5233-565X

References

Ahn, K., Cao, W., Shumko, S., & Chae, J. 2016, AAS/Solar Physics Division Meeting, 47, 2.07
Bellot Rubio, L. R., Tritschler, A., & Martínez Pillet, V. 2008, ApJ, 676, 698
Cao, W., Goode, P. R., Ahn, K., et al. 2012, in ASP Conf. Ser. 463, Second ATST-EAST Meeting: Magnetic Fields from the Photosphere to the Corona, ed. T. R. Rimmele et al. (San Francisco, CA: ASP), 291
Cao, W., Gorceix, N., Coulter, R., et al. 2010, AN, 331, 636
Dedner, A., Kemm, F., Kröner, D., et al. 2002, JCoPh, 175, 645
Deng, N., Liu, C., Yang, G., Wang, H., & Denker, C. 2005, ApJ, 623, 1195
Fisher, G. H., Bercik, D. J., Welsch, B. T., & Hudson, H. S. 2012, SoPh, 277, 59
Goode, P. R., & Cao, W. 2012, in ASP Conf. Ser. 463, Second ATST-EAST Meeting: Magnetic Fields from the Photosphere to the Corona, ed. T. R. Rimmele et al. (San Francisco, CA: ASP), 357
Hudson, H. S. 2000, ApJL, 531, L75
Hudson, H. S., Fisher, G. H., & Welsch, B. T. 2008, in ASP Conf. Ser. 383, Subsurface and Atmospheric Influences on Solar Activity, ed. R. Howe et al. (San Francisco, CA: ASP), 221
Idrees, S., Su, J., Chen, J., & Deng, Y. 2024, SoPh, 299, 91
Inoue, S. 2016, PEPS, 3, 19
Inoue, S., Hayashi, K., Magara, T., Choe, G. S., & Park, Y. D. 2014, ApJ, 788, 182
Jarolim, R., Molnar, M. E., Tremblay, B., Centeno, R., & Rempel, M. 2025, ApJ, 985, L7
Jenkins, J. M., Hopwood, M., Démoulin, P., et al. 2019, ApJ, 873, 49
Lemen, J. R., Title, A. M., Akin, D. J., et al. 2012, SoPh, 275, 17
Li, Y., Jing, J., Fan, Y., & Wang, H. 2011, ApJL, 727, L19
Liu, C., Deng, N., Liu, Y., et al. 2005, ApJ, 622, 722
Lowe, D. G. 2004, Int. J. Comput. Vision, 60, 91
Mancuso, M., Jing, J., Wang, H., & Cao, W. 2025, ApJL, 980, L4
Martínez Pillet, V. 2002, AN, 323, 342
Murabito, M., Guglielmino, S. L., Ermolli, I., et al. 2021, A&A, 653, A93
Petrie, G. J. D. 2019, ApJS, 240, 11
Rempel, M. 2011, ApJ, 729, 5
Rempel, M. 2015, ApJ, 814, 125
Sakurai, T. 1982, SoPh, 76, 301
Schou, J., Borrero, J. M., Norton, A. A., et al. 2012, SoPh, 275, 327
Siu-Tapia, A. L., Rempel, M., Lagg, A., & Solanki, S. K. 2018, ApJ, 852, 66
Solanki, S. K., & Montavon, C. A. P. 1993, A&A, 275, 283
Thomas, J. H., & Weiss, N. O. 2004, ARA&A, 42, 517
Toriumi, S., & Wang, H. 2019, LRSP, 16, 3
Uitenbroek, H. 2003, ApJ, 592, 1225
Wang, H., Deng, N., & Liu, C. 2012a, ApJ, 748, 76
Wang, H., & Liu, C. 2015, RAA, 15, 145
Wang, H., Liu, C., Qiu, J., et al. 2004, ApJL, 601, L195
Wang, S., Liu, C., Liu, R., et al. 2012b, ApJL, 745, L17
Xu, Z., Jiang, Y., Yang, J., Yang, B., & Bi, Y. 2016, ApJL, 820, L21
Yang, X., Cao, W., & Yurchyshyn, V. 2022, ApJS, 262, 55